Formation of crystallographically oriented metastable Mg_1.8Si in Mg ion-implanted Si

Yuki Kobayashi, Muneyuki Naito, Koichi Sudoh, Aurélie Gentils, Cyril Bachelet, Jérôme Bourçois

Cryst. Growth Des. 2019, 19, 7138−7142
DOI: 10.1021/acs.cgd.9b01002

Formation of crystallographically oriented metastable $Mg_{1.8}Si$ in Mg ion-implanted Si

Yuki Kobayashi,[1] Muneyuki Naito,[*,1] Koichi Sudoh,[2] Aurélie Gentils,[3] Cyril Bachelet,[3] Jérôme Bourçois[3]

[1] *Dept. of Chemistry, Konan University, Okamoto, Kobe, Hyogo 658-8501, Japan*

[2] *The Institute of Scientific and Industrial Research, Osaka University, Mihogaoka, Ibaraki, Osaka 567-0047, Japan*

[3] *Centre de Sciences Nucléaires et de Sciences de la Matière, Université Paris-Sud and CNRS-IN2P3, Université Paris-Saclay, 91405 Orsay Campus, France*

Abstract

Metastable hexagonal Mg–Si was synthesized by implanting Mg ion into Si. Single-crystalline Si(111) was irradiated with Mg ions at elevated temperature followed by thermal annealing under vacuum. Microstructural analysis with transmission electron microscopy revealed the formation of precipitates with sizes of several 10 nm in the damaged crystalline Si matrix. Using electron diffraction, the precipitates were identified as $Mg_{1.8}Si$, and the crystallographic orientation relationship between $Mg_{1.8}Si$ precipitates and Si was determined. The phase stability of $Mg_{1.8}Si$ in the Si matrix is discussed in terms of the internal stress generated during the precipitation process.

Keywords: magnesium silicides, metastable, ion implantation

Introduction

The structures, growth processes, and phase stabilities of magnesium silicides (Mg–Si) have been extensively studied from both the scientific and technological perspectives.[1–5] A primary concern related to Mg–Si stems from the attractive semiconducting properties of Mg_2Si. Cubic Mg_2Si with anti-fluorite structure is the only compound in the equilibrium binary phase diagram of Mg–Si. This compound is a narrow-gap semiconductor with a bandgap of 0.6–0.8 eV, making it a promising material for use in infrared optoelectronic devices. In addition, Mg_2Si shows potential as a thermoelectric material because of its high figure of merit resulting from the doping effect. In practical applications, Mg_2Si is highly advantageous because its constituent atoms are relatively non-toxic and abundant in the earth's crust.

In addition to the thermodynamically stable Mg_2Si, metastable Mg–Si phases have been experimentally detected or proposed computationally.[6–10] Some metastable Mg–Si phases can be prepared under high-pressure (and high-temperature) conditions via structural phase transformations from cubic Mg_2Si or solid-phase chemical reactions between Mg and Si.[11–13] The physical properties of these metastable Mg–Si phases have been investigated, and some Mg–Si phases show remarkable features. For example, the high-pressure phase of Mg_9Si_5 shows potential for use in mid-temperature thermoelectric devices.[14] Several phases of metastable Mg–Si have been identified as precipitates in Al-based alloys.[2,7–9] These types of Mg–Si have attracted particular attention in studies of the mechanical properties of Al-based alloys because the structural characteristics of the precipitates are closely related to alloy strength. The investigation of metastable Mg–Si phases is also important for the fabrication of Mg_2Si based materials because the growth of stable Mg_2Si occurs subsequent to the formation of specific metastable Mg–Si phases

such as $Mg_{1.8}Si$.[9] To better understand metastable Mg–Si phases, it is critical to clarify their formation mechanisms. In this paper, we present a new route for obtaining metastable Mg–Si using ion implantation. Using ion implantation, Baleva et al.[15] previously reported the formation of cubic Mg_2Si in Si implanted with high doses of Mg ion. However, no microscopic description was given in the investigation. In this study, we examined the microstructure of Mg ion-implanted Si using transmission electron microscopy (TEM) and electron diffraction. Based on the results, we discuss the formation and stabilization process of metastable Mg–Si in the Si matrix.

Experimental

Single-crystalline Si(111) layers on insulator substrates were employed in the present study. Ion implantation experiments were carried out with Mg ions at 10 keV and a fluence of 3.5×10^{16} cm^{-2} at 250°C and a fluence of 4.0×10^{16} cm^{-2} at −170°C using the 190 kV IRMA ion implanter of the JANNuS/SCALP facility in Orsay, France. The substrates were tilted 7° off from the incident beam direction for the sample irradiated at elevated temperatures to minimize the channeling effect, while the beam direction was parallel to the substrate surface normal for the sample irradiated at cryogenic temperature because our sample holder for low temperature irradiation did not have the tilt. However, the channeling effect was negligible because the minimum ion fluence for amorphization in crystalline Si is below 1.0×10^{15} cm^{-2} at −170°C,[16] which is sufficiently smaller than the total fluence. The implanted samples were annealed at temperatures from 300°C to 500°C at a heating rate of 100°C/min under vacuum. Cross-sectional TEM observation was carried out using a JEOL JEM-2100 electron microscope. Before observation, the as-

implanted and annealed samples were thinned using a tripod polishing technique followed by Ar-ion thinning. For analyzing diffraction patterns, electron diffraction intensities were calculated based on the kinematic approximation.

Results and discussion

Figure 1a shows a cross-sectional bright-field TEM image of the sample irradiated with 10-keV Mg ions at 250°C. Based on the image contrast, Mg-ion irradiation resulted in the formation of a 10-nm-thick amorphous top layer along with a defective crystalline region at depths between 10 and 70 nm from the surface. Monte Carlo simulation using SRIM code[17] was used to estimate the concentration of Mg in the Si target. Figure 1a shows the Mg profile as a function of depth. The maximum Mg concentration of approximately 20 at.% was observed at a depth of 20 nm. Precipitates formed within the crystalline matrix in the region with high Mg concentration. Figure 1b shows a typical high-resolution TEM image of the precipitate (indicated by the arrow), and the inset shows the fast Fourier transform pattern obtained from the area outlined by the dotted square. The periods and crossing angles of the lattice fringes in the precipitate are not consistent with those observed in crystalline Si. In addition to the spots related to Si, the fast Fourier transform pattern shows spots associated with the precipitates, as indicated by the arrows in the inset. The lattice spacings estimated from these additional spots (e.g., 0.20 and 0.36 nm) do not correspond to either Si or Mg crystals, indicating that Mg reacted with Si during ion implantation to form Mg–silicide precipitates in the Si matrix.

Post-implantation annealing induced microstructural changes in the ion-

implanted region. Figure 2a shows a bright-field TEM image of the sample annealed at 500°C for 5 min. The topmost amorphous layer was slightly recrystallized at the amorphous–crystalline interface via solid-phase epitaxy, and precipitate growth was observed in the defective crystalline region. To more clearly detect the precipitates, dark-field TEM imaging of the annealed sample was carried out. Figure 2b shows an electron diffraction pattern of the damaged region including precipitates. The incident electron beam was aligned parallel to the $[11\bar{2}]$ zone axis of Si; thus, the 111 and $2\bar{2}0$ spots of Si are clearly observed in the diffraction pattern. Additional weak spots arising from the precipitates are observed, as marked by the dotted circle in Figure 2b, and are used for dark-field TEM imaging. Figure 2c shows a dark-field TEM image taken from the same area as the bright-field TEM image in Figure 2a. The dark-field image clearly indicates that spherically shaped precipitates with sizes of 10–20 nm were embedded in the crystalline Si matrix. The precipitates were most frequently observed at depths of 20–30 nm, comparable to the depth of the region with high Mg concentration, as estimated by SRIM calculation.

The crystalline phase of the precipitates was evaluated using electron diffraction. Figures 3a and b show typical diffraction patterns obtained from the damaged region viewed along the Si$[11\bar{2}]$ and Si$[10\bar{1}]$ zone axis directions, respectively. The diffraction pattern in Figure 3b was obtained by tilting the sample by 30 degrees around the g_{111} reciprocal vector of Si after obtaining the diffraction pattern in Figure 3a in the same area. The reflections of the precipitates appear periodically in both diffraction patterns, as indicated by the arrows in Figure 3a and b. This indicates the existence of a specific crystallographic orientation relationship between the precipitates and the Si matrix. Further details regarding this relationship are discussed later. Based on an examination of

the reflections, the diffraction patterns of the precipitates agree well with those of metastable $Mg_{1.8}Si$. Figure 3c and d show the simulated electron diffraction patterns of $Mg_{1.8}Si$ viewed along the [110] and [210] directions based on the crystal structure proposed by Vissers et al.[18] The structural model was built for the $Mg_{1.8}Si$ precipitate formed in Al–Mg–Si alloys using both experimental and theoretical data. In the model, the unit cell of $Mg_{1.8}Si$ is hexagonal (space group: $P6_3/m$) with lattice parameters of a = 0.715 nm and c = 1.215 nm. As a result of disordering of Si atoms and vacancies at the 00z positions, the unit cell can be replaced by an averaged structure with lattice parameters of a = 0.715 nm and $c' = c/3$ = 0.405 nm. In this study, no superlattice reflections related to the ordering of Si and vacancies were observed, indicated that the disordered crystalline phase of $Mg_{1.8}Si$ was formed under the present experimental conditions. It should be noted that the precipitation of cubic Mg_2Si was also observed in the annealed sample, whereas no Mg_2Si was found in the as-implanted sample.

Several metastable Mg–Si precipitates, including $Mg_{1.8}Si$, are known to be formed in Al–Mg–Si alloys. However, to the best of our knowledge, $Mg_{1.8}Si$ formation in the crystalline Si matrix has not been reported before now. Therefore, it is worth discussing the phase stability of the $Mg_{1.8}Si$ precipitates observed in this study. As reported by Ji et al.,[13] a bulk compound related to $Mg_{1.8}Si$ and referred to as Mg_9Si_5 can be synthesized under high-pressure and high-temperature conditions. The authors reported that the obtained hexagonal Mg_9Si_5 (lattice parameters of a = 1.2411 nm and c = 1.2345 nm) corresponds to a superstructure of $Mg_{1.8}Si$, and a phase transformation from Mg_9Si_5 to Mg_2Si occurred upon annealing under Ar atmosphere. On the other hand, the first-principles calculations[5] show that $Mg_{1.8}Si$ is a pressure-stabilized Mg–Si compound. Based on these results, the $Mg_{1.8}Si$ observed in the present study was stabilized by the

pressure generated by internal stress.

The internal stress generated in Mg ion-implanted Si can be classified into two types: ion implantation-induced stress and coherency stress. In general, the ion-implanted region is compressed because it attempts to expand as a result of void formation and the presence of implanted ions; however, the expansion is suppressed by the non-ion-implanted region. This situation gives rise to compressive stress in the ion-implanted region.[19–21] The compressive stress increases with increasing ion energy and fluence of the implanted ions; the compressive stress then decreases after reaching its maximum value with the growth of the amorphous region in the target. For Si single crystals, the maximum stress induced by ion implantation was reported to be on the order of 10^8–10^9 Pa.[22,23] The values are close to the pressure at which metastable Mg–Si phases are formed in high-pressure experiments. On the other hand, the coherency stress arising from the lattice mismatch between the precipitate and the matrix should also be considered. When precipitates grow in the matrix, coherent and semi-coherent boundaries are often formed to reduce the interfacial energy and strain energy. As a result, specific crystallographic orientations between precipitates and matrixes are observed. For example, $Mg_{1.8}Si$ precipitates are grown with the *c*-axes along the Al<001> directions in the Al–Mg–Si alloys since the value of *c*' (0.405 nm) in disordered $Mg_{1.8}Si$ is almost identical to {001} plane spacing of Al. Thus, the following crystallographic orientation relationship can be observed[18]: Al<001> // $Mg_{1.8}Si$[001] with Al<$\bar{3}$10> // $Mg_{1.8}Si$[100]. As mentioned above, the $Mg_{1.8}Si$ precipitates observed in this study exhibited specific crystallographic orientations in the Si matrix, and the orientation relationship between $Mg_{1.8}Si$ and Si was determined by electron diffraction to be Si(111) // $Mg_{1.8}Si$(001) with Si[11$\bar{2}$] // $Mg_{1.8}Si$[110]. The atomic arrangement of $Mg_{1.8}Si$ on the Si(111) plane in this

crystallographic orientation relationship is shown in Figure 4. In this configuration, $Mg_{1.8}Si$ and Si show relatively large lattice mismatches of approximately 7.6% in both the Si[$1\bar{1}0$] and Si[$11\bar{2}$] directions. The positive mismatches on the Si(111) plane give rise to the compressive stress.

To investigate the effect of compressive stress on the formation of $Mg_{1.8}Si$ in crystalline Si, we examined Mg–Si formation in a disordered Si matrix (i.e., amorphous Si). Most of the ion beam-induced stress is relieved in amorphous Si,[22] and there is no coherency between the precipitates and the matrix. Figure 5a shows the cross-sectional TEM image of the 10-keV Mg ion-implanted Si(111) at cryogenic temperature (−170°C). A fully amorphized Si layer with a thickness of 55 nm was formed in the as-implanted sample as the damage recovery was insufficient under cryogenic temperature. After annealing at 300°C for 30 min, the sample remained amorphous, as shown in Figure 5b. However, precipitation was observed in the amorphous Si, as indicated by the arrow in Figure 5b. A high-resolution TEM image of the precipitates is shown in Figure 5c, and a magnified TEM image is also shown in the inset. It is found that the lattice fringe spacing of ~0.37 nm is in good agreement with the Mg_2Si(111) interplanar spacing. Electron diffraction in Figure 5d revealed that the precipitates were a polycrystalline form of cubic Mg_2Si, and no hexagonal $Mg_{1.8}Si$ was detected in the amorphous matrix. The discontinuous Debye-Scherrer rings in Figure 5d are due to the small number of precipitates. Electron diffraction intensity profiles along directions 1 and 2 in Figure 5d are shown in Figure 5e. The peak positions in the intensity profiles were well explained by the interplanar spacings of Mg_2Si, which are indicated by bars in Figure 5e. This result suggests that the formation of $Mg_{1.8}Si$ is more favorable than that of Mg_2Si under compressive stress. In the crystalline Si matrix, Mg_2Si was formed after $Mg_{1.8}Si$, as

described above. Mg_2Si formation is thought to be promoted by the relaxation of compressive stress resulting from post-implantation thermal treatment.[23] Further experiments are necessary to clarify the effect of ion implantation conditions, volume of the matrix (the thickness of Si), and post-implantation annealing on the structural phase stability of $Mg_{1.8}Si$ and phase transformation process of Mg–Si compounds in the crystalline Si matrix.

Conclusions

The microstructures of Mg ion-implanted Si were investigated by cross-sectional TEM and electron diffraction. Ion implantation at elevated temperature induced the solid-phase reaction between Si and Mg along with the growth of metastable $Mg_{1.8}Si$. The $Mg_{1.8}Si$ precipitates are crystallographically oriented with respect to the Si matrix. The orientation relationship between $Mg_{1.8}Si$ and Si was determined to be Si(111) // $Mg_{1.8}Si$(001) with Si[$11\bar{2}$] // $Mg_{1.8}Si$[110]. The formation of $Mg_{1.8}Si$ precipitates in the crystalline Si matrix was attributed to ion implantation-induced stress and/or coherency stress.

Acknowledgment

This work was supported in part by the Japan Science and Technology Agency, Crest.

References

(1) Mahan, J. E.; Vantomme, A.; Langouche, G.; Becker, J. P. Semiconducting Mg_2Si thin films prepared by molecular-beam epitaxy. *Phys. Rev. B* **1996**, *54*, 16965–16971.

(2) Zandbergen, H. W.; Andersen, S. J.; Jansen, J. Structure determination of Mg_5Si_6 particles in Al by dynamic electron diffraction Studies. *Science* **1997**, *277*, 1221–1225.

(3) Wang, Y.; Wang, X. N.; Mei, Z. X.; Du, X. L.; Zou, J.; Jia, J. F.; Xue, Q. K.; Zhang, X. N.; Zhang, Z. Epitaxial orientation of $Mg_2Si(110)$ thin film on Si(111) substrate. *J. Appl. Phys.* **2007**, *102*, 126102.

(4) Opahle, I.; Madsen, G. K. H.; Drautz, R. High throughput density functional investigations of the stability, electronic structure and thermoelectric properties of binary silicides. *Phys. Chem. Chem. Phys.* **2012**, *14*, 16197–16202.

(5) Huan, T. D. Pressure-stabilized binary compounds of magnesium and silicon. *Phys. Rev. Mater.* **2018**, *2*, 023803.

(6) Cannon, P.; Conlin, E. T. Magnesium compounds: New dense phases. *Science* **1964**, *145*, 487–489.

(7) Jacobs, M. H. The structure of the metastable precipitates formed during ageing of an Al-Mg-Si alloy. *Philos. Mag.* **1972**, *26*, 1–13.

(8) Matsuda, K.; Sakaguchi, Y.; Miyata, Y.; Uetani, Y.; Sato, T.; Kamio, A.; Ikeno, S. Precipitation sequence of various kinds of metastable phases in Al-1.0mass% Mg_2Si-0.4mass% Si alloy. *J. Mater. Sci.* **2000**, *35*, 179–189.

(9) Ravi, C.; Wolverton, C. First-principles study of crystal structure and stability of Al–Mg–Si–(Cu) precipitates. *Acta Mater.* **2004**, *52*, 4213–4227.

(10) Huan, T. D.; Tuoc, V. N.; Le, N. B.; Minh, N. V.; Woods, L. M. High-pressure

phases of Mg_2Si from first principles. *Phys. Rev. B* **2016**, *93*, 094109.

(11) Hao, J.; Zou, B.; Zhu, P.; Gao, C.; Li, Y.; Liu, D.; Wang, K.; Lei, W.; Cui, Q.; Zou, G. *In situ* X-ray observation of phase transitions in Mg_2Si under high pressure. *Solid State Com.* **2009**, *149*, 689–692.

(12) Ren, W.; Han, Y.; Liu, C.; Su, N.; Li, Y.; Ma, B.; Ma, Y.; Gao, C. Pressure-induced semiconductor–metal phase transition in Mg_2Si. *Solid State Com.* **2012**, *152*, 440–442.

(13) Ji, S.; Imai, M.; Zhu, H.; Yamanaka, S. Structural characterization of magnesium-based compounds Mg_9Si_5 and Mg_4Si_3Al (superconductor) synthesized under high pressure and high temperature conditions. *Inorg. Chem.* **2013**, *52*, 3953–3961.

(14) Singh, V.; Pulikkotil, J. J.; Auluck, S. Mg_9Si_5: a potential non-toxic thermoelectric material for mid-temperature applications. *RSC Adv.* **2016**, *6*, 62445–62450.

(15) Baleva, M.; Zlateva, G.; Atanassov, A.; Abrashev, M.; Goranova, E. Resonant Raman scattering in ion-beam-synthesized Mg_2Si in a silicon matrix. *Phys. Rev. B* **2005**, *72*, 115330.

(16) Pelaz, L.; Marqués, L. A.; Barbolla, J. Ion-beam-induced amorphization and recrystallization in silicon. *J. Appl. Phys*. **2004**, *96*, 5947-5976.

(17) Ziegler, J. SRIM & TRIM software; http://www.srim.org/.

(18) Vissers, R.; van Huis, M. A.; Jansen, J.; Zandbergen, H. W.; Marioara, C. D.; Andersen, S. J. The crystal structure of the β’ phase in Al–Mg–Si alloys. *Acta Mater.* **2007** *55*, 3815–3823.

(19) Krefft, G. B.; EerNisse, E. P. Volume expansion and annealing compaction of ion-bombarded single-crystal and polycrystalline α-Al_2O_3. *J. Appl. Phys.* **1978**, *49*, 2725–2730.

(20) Madakson, P.; Angilello, J. Stresses and radiation damage in Ar^+ and Ti^+ ion-

implanted silicon. *J. Appl. Phys.* **1987**, *62*, 1688–1693.

(21) Davis, C. A. A simple model for the formation of compressive stress in thin films by ion bombardment. *Thin Solid Films* **1993**, *226*, 30–34.

(22) Volkert, C. A. Stress and plastic flow in silicon during amorphization by ion bombardment. *J. Appl. Phys.* **1991**, *70*, 3521–3527.

(23) Zhang, X. W.; Wong, S. P.; Cheung, W. Y. Effects of stress on electrical transport properties of nickel silicide thin layers synthesized by Ni-ion implantation. *J. Appl. Phys.* **2002**, *92*, 3778–3783.

(24) Naito, M.; Ishimaru, M.; Hirotsu, Y.; Valdez, J. A.; Sickafus, K. E. Transmission electron microscopy study on ion-beam-synthesized amorphous Fe–Si thin layers. *Appl. Phys. Lett.* **2005**, *87*, 241905.

(25) Villars, P.; Cenzual, K. Pearson's Crystal Data−Crystal Structure Database for Inorganic Compounds (on DVD), Release 2016/17; ASM International: Materials Park, OH, 2016.

Figure captions

Figure 1. (a) Cross-sectional bright-field TEM image and (b) high-resolution TEM image of the sample irradiated with 10-keV Mg ions at 250°C. The Mg concentration as a function of depth estimated by Monte Carlo simulation is shown in (a). A fast Fourier transform pattern obtained from the high-resolution TEM image is shown in (b).

Figure 2. (a) Cross-sectional bright-field TEM image and (b) corresponding selected-area electron diffraction pattern of the annealed sample. The incident electron beam was aligned along the $[11\bar{2}]$ zone axis of Si in (a) and (b). The diffraction spot indicated by the dotted circle in (b) was used for dark-field imaging. The resultant dark-field image is shown in (c).

Figure 3. Electron diffraction patterns obtained from the Mg ion-implanted region in the annealed sample viewed along the (a) $[11\bar{2}]$ and (b) $[10\bar{1}]$ zone axes of Si. Simulated electron diffraction patterns of $Mg_{1.8}Si$ viewed along the (c) [110] and (d) [210] directions.

Figure 4. Schematic diagram showing the atomic arrangement of $Mg_{1.8}Si$ on the Si(111) plane with a crystallographic orientation relationship of Si(111) // $Mg_{1.8}Si(001)$ with $Si[11\bar{2}]$ // $Mg_{1.8}Si[110]$.

Figure 5. Cross-sectional bright-field TEM images of the Mg ion-implanted Si(111) at −170°C: (a) as-implanted and (b) 300°C-annealed samples. (c) A high-resolution TEM image of the Mg–Si precipitates and magnified TEM image is shown in the inset. (d)

Electron diffraction pattern of the Mg–Si precipitates, including reflections of both crystalline and amorphous Si. (e) Electron diffraction intensity profiles along directions 1 and 2 in (d) as a function of d^{-1} (d: interplanar spacing). For comparison, the intensity profile from the amorphous Si (a-Si)[24] together with the bars indicating the diffraction peak positions from Mg_2Si,[25] $Mg_{1.8}Si$,[18] and Si[25] are shown in (e); the reflections with relative electron diffraction intensities (with respect to the maximum intensity) less than 5% are indicated by shorter bars, while those less than 1% are not shown.

For Table of Contents Use Only

Formation of crystallographically oriented metastable $Mg_{1.8}Si$ in Mg ion-implanted Si

Yuki Kobayashi[1], Muneyuki Naito[1], Koichi Sudoh[2], Aurélie Gentils[3], Cyril Bachelet[3], Jérôme Bourçois[3]

[1] *Dept. of Chemistry, Konan University, Okamoto, Kobe, Hyogo 658-8501, Japan*

[2] *The Institute of Scientific and Industrial Research, Osaka University, Mihogaoka, Ibaraki, Osaka 567-0047, Japan*

[3] *Centre de Sciences Nucléaires et de Sciences de la Matière, Université Paris-Sud and CNRS-IN2P3, Université Paris-Saclay, 91405 Orsay Campus, France*

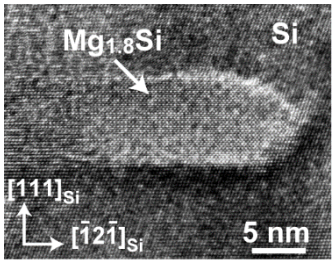

Synopsis

Metastable $Mg_{1.8}Si$ nanocrystals are grown in Mg ion-implanted single-crystalline Si at elevated temperature. A specific crystallographic orientation relationship between the $Mg_{1.8}Si$ nanocrystals and Si matrix was revealed by high-resolution TEM and electron diffraction. The structural phase stability of the metastable phase is discussed in the context of internal stress.

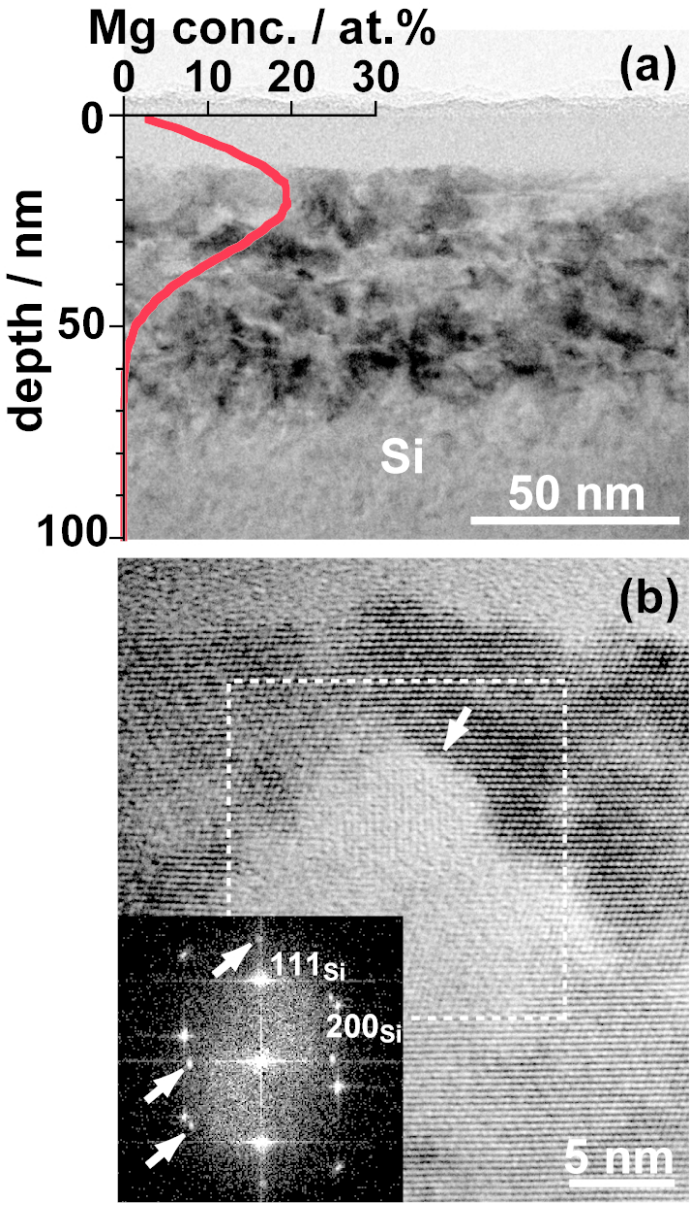

Figure 1. (a) Cross-sectional bright-field TEM image and (b) high-resolution TEM image of the sample irradiated with 10-keV Mg ions at 250oC. The Mg concentration as a function of depth estimated by Monte Carlo simulation is shown in (a). A fast Fourier transform pattern obtained from the high-resolution TEM image is shown in (b).

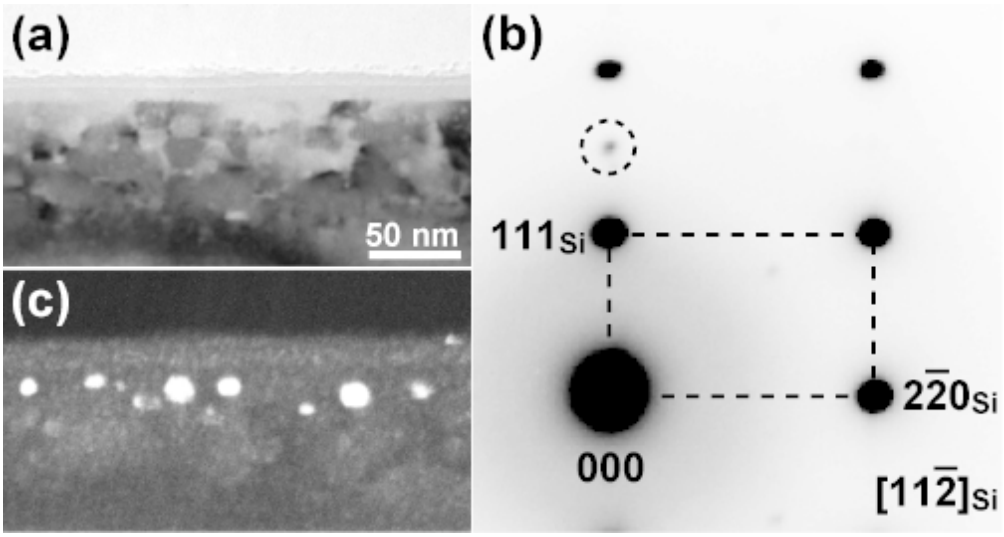

Figure 2. (a) Cross-sectional bright-field TEM image and (b) corresponding selected-area electron diffraction pattern of the annealed sample. The incident electron beam was aligned along the [11–2] zone axis of Si in (a) and (b). The diffraction spot indicated by the dotted circle in (b) was used for dark-field imaging. The resultant dark-field image is shown in (c).

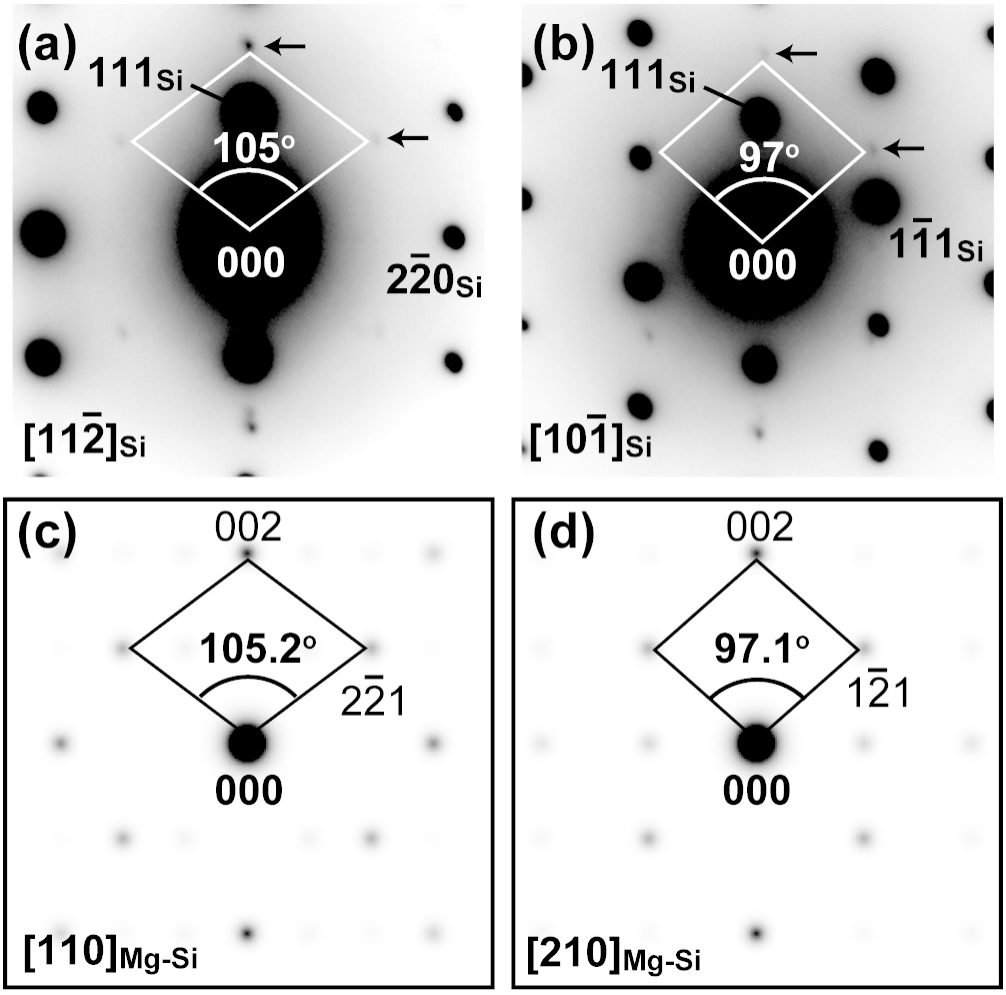

Figure 3. Electron diffraction patterns obtained from the Mg ion-implanted region in the annealed sample viewed along the (a) [112(−)] and (b) [101(−)] zone axes of Si. Simulated electron diffraction patterns of Mg1.8Si viewed along the (c) [110] and (d) [210] directions.

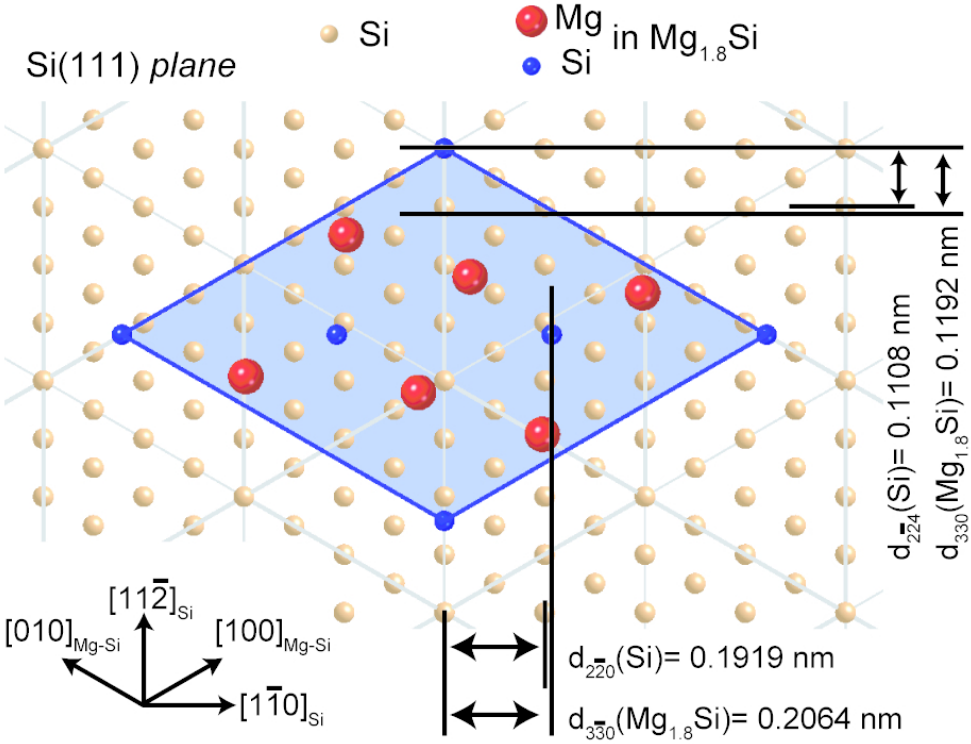

Figure 4. Schematic diagram showing the atomic arrangement of $Mg_{1.8}Si$ on the Si(111) plane with a crystallographic orientation relationship of Si(111) // $Mg_{1.8}Si$(001) with Si[11–2] // $Mg_{1.8}Si$[110].

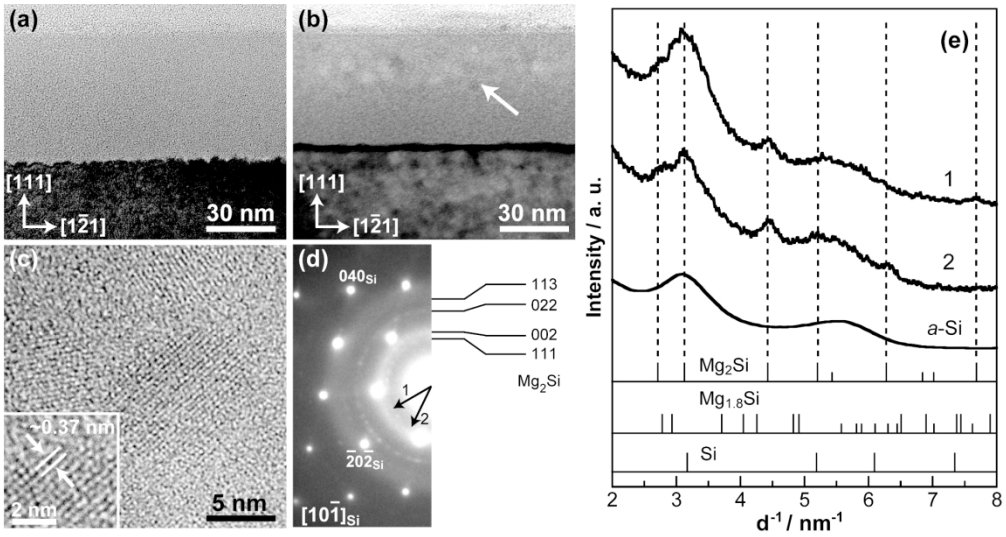

Figure 5. Cross-sectional bright-field TEM images of the Mg ion-implanted Si(111) at −170oC: (a) as-implanted and (b) 300oC-annealed samples. (c) A high-resolution TEM image of the Mg–Si precipitates and magnified TEM image is shown in the inset. (d) Electron diffraction pattern of the Mg–Si precipitates, including reflections of both crystalline and amorphous Si. (e) Electron diffraction intensity profiles along directions 1 and 2 in (d) as a function of d-1 (d: interplanar spacing). For comparison, the intensity profile from the amorphous Si (a-Si)24 together with the bars indicating the diffraction peak positions from Mg2Si,25 Mg1.8Si,18 and Si25 are shown in (e); the reflections with relative electron diffraction intensities (with respect to the maximum intensity) less than 5% are indicated by shorter bars, while those less than 1% are not shown.